Journal of Engineering and Technological Sciences

Research Paper

Analysis of Mechanical Properties and Acoustic-Thermal Response Characteristics of Water-Soaked Gabbro

Zhi Bin[1], Xu Xiaojing[*2,3], Wang Qijie[2,3], Li Changwei[1], Zhang Yutao[2], Song Zhanping[2,3], & Kang Baoxiang[4]

[1]China Road & Bridge Corporation, Beijing 100011, China
[2]School of Civil Engineering, Xi'an University of Architecture and Technology, Xi'an 710055, China
[3]Shaanxi Key Laboratory of Geotechnical and Underground Space Engineering, Xi'an 710055, China
[4]Xi'an Vocational University of Automobile, School of Traffic Engineering, Xi'an 710600, China

*Corresponding author: xuxiaojing_789@163.com

Abstract Shaanxi Key Laboratory of Geotechnical and Underground Space Engineering, Xi'an 710055

With the national strategy being implemented and taking root in the infrastructure sector, the increased of water erosion in rock formations during railway construction has risen significantly, posing a considerable risk to the stability and structural integrity of engineering rock formations. Consequently, there is a critical need to investigate how water influences the mechanical properties of gabbro. Uniaxial compression experiments were performed on both arid and water-soaked gabbro pieces, simultaneously monitoring the characteristics of acoustic emission (AE) and infrared radiation (IR) response. The Particle Flow Code (PFC) was utilized to examine the microscopic processes of crack propagation, coalescence, and damage progression in the rock pieces. Observations show that water considerably impacts the mechanical characteristics of gabbro. In comparison to arid pieces, the peak strength of water-soaked pieces showed a reduction of 4.98%, while the elastic modulus was diminished by 16.5%. The failure behavior of the pieces shifted progressively from tensile splitting in the arid condition to tensile-shear failure. Both arid and water-soaked pieces displayed pre-shock-main shock patterns in their AE parameters. By creating a damage variable based on cumulative AE ring counts, the damage evolution of the pieces was categorized into three phases: incipient damage, steady damage, and expedited damage phases. Throughout loading and fracturing, the AIRT (average infrared radiation temperature) curve exhibited a downward trend, followed by a sharp rise, featuring a "V"-shaped turn prior to piece failure. The evolution of AIRT in water-soaked pieces showed strong alignment with stress variations. Numerical simulations using PFC revealed that the quantity of shear cracks in water-soaked pieces increased, constituting a larger share of the total cracks in contrast to arid pieces. After loading, water-soaked pieces generated more strong force chains, with the load borne by bonds gradually increasing *crack evolution*, making them more susceptible to failure.

Keywords: *acoustic emission; crack evolution; infrared radiation; mechanical behaviors; water-soaked gabbro.*

Introduction

With the in-depth advancement of the Western Development Strategy and the "Belt and Road" Initiative, railway construction in western China and countries along the Initiative has embraced unprecedented development opportunities (Huang et al. 2021; Huang and Yu, 2022). Nevertheless, amid the large-scale construction of railway projects, the issue of groundwater erosion on rock masses has grown increasingly prominent, emerging as a pivotal factor that constrains the stability of engineering rock masses and structural safety (Chen et al. 2019; Xu et al. 2024). Consequently, conducting systematic research into the mechanical behavior of hard rocks under water-soaked conditions holds significant practical importance for safeguarding the safety and stability of surrounding rocks in projects like tunnels and road cuttings.

Water stands as a core factor undermining the mechanical properties of rock materials, capable of substantially reducing key parameters such as rock strength and elastic modulus. The deformation characteristics and damage evolution of sandstone (Cheng et al., 2022, 2024) and limestone (Fan et al., 2022) under water-soaked conditions have been extensively studied by means of AE (Song et al., 2024) and IR detection technology. The red and cyan sandstones were subjected to monotonous and cyclical compression experiments in both arid and water-soaked conditions by Zhu et al. (2024). They also observed periodic pressure levels using AE to increase peak strain and drastically decrease peak stress

Copyright by authors ©2026 Published by IRCS - ITB

ISSN: 2337-5779
DOI: 10.5614/j.eng.technol.sci.2026.58.4.2

in both arid and water-soaked rocks, with the effects being more noticeable in the latter case.The response mechanism and control elements of the dominat frequency-amplitude sign of AE were revealed by Zhang et al. (2023) using low-field nuclear magnetic resonance (nMR) methods and AE. Observations show that there are three phases of water-induced sandstone structural damage: incipient, steady development, and calm. Water content has a reverse relationship with mechanical strength and a proportional relationship with surface roughness of crystal fracture. In the process of sandstone fracture, the AE spectrum responds in four ways. Xiao et al. (2019) employed AE, average infrared temperature, and an infrared thermal imaging system for monitoring. They discovered that the integration of infrared and AE techniques can mirror the early warning sign of the structural instability of coal pieces. The emergence of the AE signal occurs earlier than the appearance of the infrared anomaly point, which serves as the early warning sign of coal structure instability. Muhammad Khan et al. (2023) examined the impact of shear load and water content on rock deformation and fracture. They found that a rise in water content decreased the AE and strain of the material while increasing the shear stress of the material. Cao et al. (2022) carried out infrared observation tests on both arid sandstone and water-soaked sandstone. It was revealed that water-soaked not merely undermines the mechanical characteristics of rocks but likewise gives a boost to infrared emissions that can function as stress precursors. Moreover, a model of rocks based on infrared ray was also created. Liu and his research team (2018) investigated the result brought by water content on rock burst by means of an indoor sandstone tunnel model experiment. It was determined that the quiescent phase of the AE event rate and the sudden, significant increase in the AE energy rate could be seen as the harbingers of rock burst.Water also promotes the infrared temperature effect of the saturation model. The sudden change of tunnel surrounding rock temperature can be used as a spatial scale precursor of rock burst. In addition, scholars have also combined neural networks to analyze and optimize AE and IR(Ma et al., 2024). With advancements in computing technology, numerical methods have become increasingly pivotal in the field of rock engineering. Researchers have employed the particle discrete element software PFC to investigate the influence of microstructure on the mechanical properties and failure characteristics of rocks. Yu et al. (2025) utilized PFC3D software to establish numerical models of sandstone with varying water contents. By integrating uniaxial compression tests with energy calculation principles, they systematically examined the mechanical degradation laws and energy evolution characteristics of sandstone under water-rock interaction. Li et al. (2025) performed numerical simulations using particle flow field simulation software, systematically analyzing changes in parameters such as water-sediment displacement, flow velocity, flow rate, energy loss, porosity, and effective permeability within rock formations and collapse zones. Zhao et al. (2021) conducted a systematic analysis of the microcrack evolution process, rock failure modes, and AE characteristics of red sandstone under different water contents through a combination of uniaxial compression tests and PFC2D numerical simulations.

At present, the research on gabbro is focused on the impact of temperature on its mechanical characteristics.(Ge & Sun, 2021; Zhou et al., 2023; Liu et al., 2024), and the impact of water content on gabbro is not clear. Therefore, In this thesis, the indoor uniaxial compressive experimenting of gabbro under both arid and water-soaked states is conducted, and the AE and IR monitoring are executed in parallel to explore the mechanical attributes and breakdown modalities of arid and wet gabbro. The failure precursors of gabbro are identified by AE signals and IR images. The Discrete Element Method (DEM) is used to simulate arid and wet gabbro, and the progression of crack development during the failure process of rock pieces is revealed from a microscopic point of view. To offer a scientific foundation for the assessment and reinforcement of the stability of surrounding rock engineering, and facilitate the secure and high-efficiency advancement of railway engineering construction in China's western region as well as in the nations along the Belt and Road Initiative.

Uniaxial Compression Experiment

Reliable power supply is essential for national development, and uninterrupted electricity access significantly supports industrial growth, public services, and living standards. Numerous researchers have examined the causes of blackouts and the importance of maintaining voltage levels within permissible limits to avoid equipment damage and system instability (Nonthapot et al., 2025).

Voltage regulation and power loss reduction have been addressed through various strategies, including the use of On Load Tap Changer (OLTC) transformers, reactive power compensation, and advanced control systems like automatic voltage regulators and FACTS devices (Karuppiah et al., 2020; Xu & Taylor, 2008). These methods aim to maintain a stable voltage profile across all parts of the distribution network.

However, one of the less complex but highly impactful factors influencing system performance is the physical location of distribution transformers. Proper placement of transformers can significantly reduce technical losses and voltage drops in the network. Several studies emphasize that installing transformers close to load centers minimizes power losses and improves voltage quality (Hegde et al., 2014; Pinzón et al., 2020) Optimal transformer location is influenced

DOI: 10.5614/j.eng.technol.sci.2026.58.4.2

by several criteria, such as proximity to load demand, accessibility, minimal land use, and environmental safety(Sebestyén, 2021)(Chamandoust et al., 2020).

Despite the existing body of work, some distribution networks—particularly in developing regions—lack the application of these planning principles. For instance, in Duhok city, improper transformer placement without feasibility studies has led to inefficiencies in voltage delivery and increased technical losses. Similar issues have been reported in other studies focusing on unplanned expansion and weak infrastructure in distribution systems, where transformer relocation has proven effective in performance improvement.

Therefore, this research contributes to the literature by evaluating the impact of transformer relocation in a real-world setting. It builds on previous studies by focusing on measurable improvements in voltage profile and power loss reduction when transformers are installed closer to load centers.

Uniaxial Compression Experiment

Rock Piece Making and Experiment Devices

The rock material used in the experiment is slightly weathered gabbro of Jinning period from Panzhihua Sunshine Tunnel in Sichuan Province. According to the ISRM experiment procedures, a regular cylindrical part having a diameter of 50 mm and standing 100 mm in height is processed, and there aren't any noticeable flaws on the exterior of the rock piece. In order to reduce the terminal effect of the rock piece during the experiment, the flatness of the rock piece's end surface is regulated within ± 0.02 mm to ensure that the terminal face is at a right angle to the axis of the rock piece. After the rock piece is processed, its weight is measured, and the rock piece with small mass difference is selected, as shown in Figure 1.

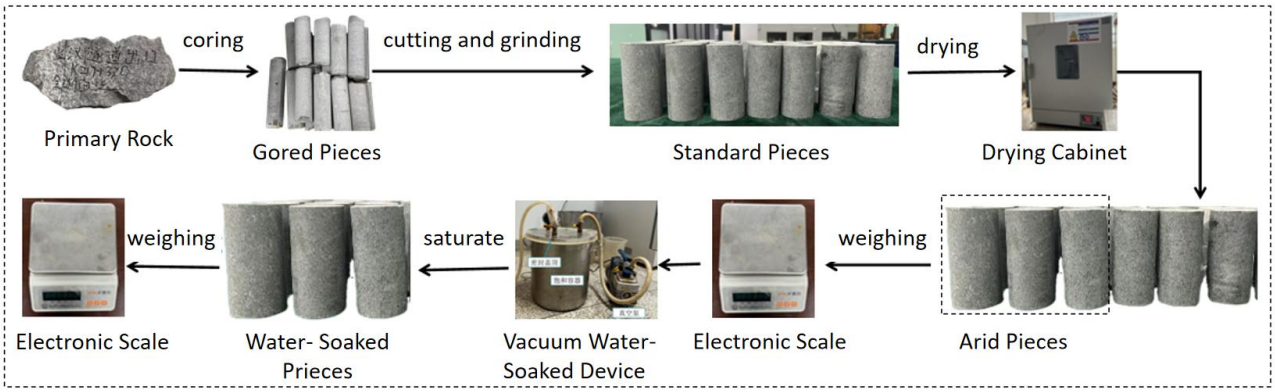

Figure 1 Pieces Preparation and Treatment Process for Arid and Water-Soaked Rock Pieces.

There is a large amount of groundwater in the tunnel area, so the influence of water is considered in the experiment. A total of six rock pieces were grouped into two groups (group A and group B) on average. The two groups of rock pieces underwent the ariding process. After the ariding treatment was completed, the group B was then treated with soaking water. (1) ariding treatment of rock pieces : Two sets of rock pieces were put into a ariding oven set at 105 ℃ and left there for 24 hours, and the weight of rock pieces was measured after cooling. (2) Saturation treatment of rock pieces : The rock pieces of group B were immersed in the ionic water of the vacuum saturation cylinder, and the quality of the rock pieces was measured every other time. After soaking for 24 h, the quality of the rock pieces did not change, and the rock pieces were considered to be water-soaked. After saturation treatment, it was found that the water saturation level of the rock pieces was between 0.43% and 0.56%.

The loading device employed in this experiment was the TAW-2000 rock triaxial testing system, which primarily consists of an axial loading/unloading system, a confining pressure loading unit, a deformation measurement module, and a computer control system. This equipment supports two loading control modes: stress control and displacement control, with a maximum load capacity of 600 kN. It enables real-time acquisition and recording of load, stress, and strain data, and its physical configuration is illustrated in Figure 2. Concurrently, acoustic emission (AE) and infrared (IR) data were collected using a SAEU2S-1016-4 multi-channel AE monitor and a FLIR A655sc infrared thermal imager, respectively. Specifically, the AE monitoring was performed with the SAEU2S-1061-4 multi-channel acoustic emission testing system

manufactured by Beijing Shenghua Technology Co., Ltd. For this experiment, the AE acquisition threshold was set to 40 dB, with a sampling interval of 400 μ s and a sampling frequency of 1000 kHz. The infrared detection equipment selected was the FLIR-A300 thermal infrared imager produced by FLIR Systems (USA). Key specifications of this imager are as follows: dimensions of 170 mm × 70 mm × 70 mm, an operating temperature range of -15~+50°C, a thermal sensitivity of 0.001°C, a pixel acquisition frequency of 30 Hz, a continuous digital zoom range of 1~8×, a thermal infrared resolution of 320×240 pixels, a detector time constant of 12 ms, and a measurement accuracy of ±2°C.

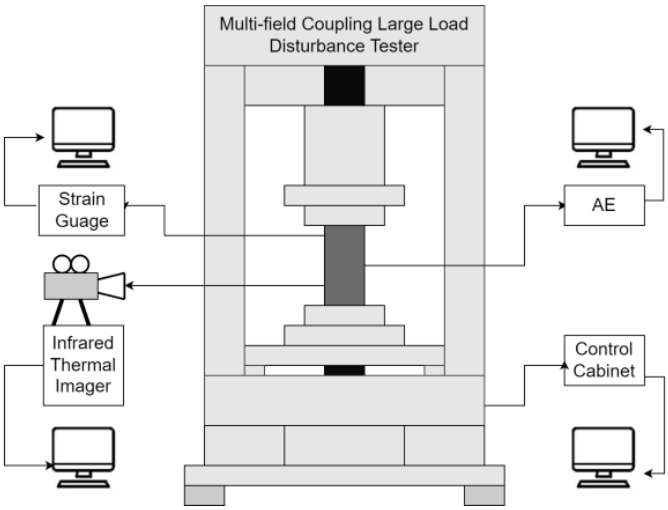

Figure 2 TAW-2000 rock triaxial experiment system.

Mineral Composition Analysis

The strength and deformation of the rock are strongly linked to the mineral composition. X-ray diffraction (XRD) is utilized to study the mineral makeup and the characteristics of the interior pore framework of the gabbro. The results from the mineral composition experiment are presented in Figure 3. The rock piece belongs to the medium composed of non-clay mineral compounds and clay mineral compounds. The content of non-cohesive minerals is high, accounting for 68.2 %, which constitutes the main frame of rock bearing and transmitting load. The proportion of clay minerals in rock pieces is 31.8 %. The existence of clay minerals will weaken the connection and integrity between rock particles, causing the decline of rock strength and elastic modulus. Clay minerals have strong hydrophilicity, and water molecules are easily adsorbed on their surfaces and infiltrate between layers, causing clay minerals to expand and further weakening the bonding force between particles.

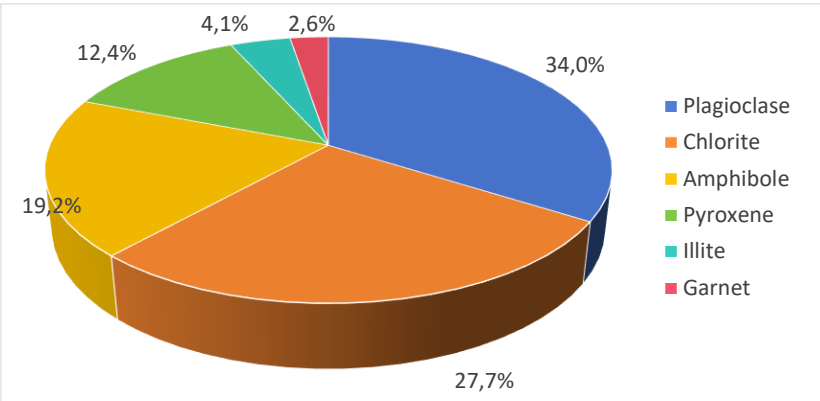

Figure 3 Mineral composition and proportion of gabbro.

Experiment Scheme

Uniaxial compression experiments were performed out on arid rock pieces G-D-1, G-D-2, G-D-3 and water-soaked rock pieces B-D-1, B-D-2, B-D-3 (where G represents arid, B represents water-soaked, D represents uniaxial loading, serial numbers 1, 2, 3 represent three repeated experiments in each group). Based on the experiment outcomes of rock saturation, the water content is calculated. The results of related physical parameters are displayed in Table 1.

DOI: 10.5614/j.eng.technol.sci.2026.58.4.2

Table 1 Grouping and physical parameters.

state	Rock piece	Quality before ariding(g)	soaking time(h)	rate of water content
arid rock pieces	G-D-1	579.24	0	0
	G-D-2	581.5	0	0
	G-D-3	581.68	0	0
water-soaked rock pieces	B-D-1	579.07	24	0.43
	B-D-2	580.63	24	0.51
	B-D-3	581.29	24	0.56

The stress-controlled loading was used in the experiment. Firstly, a pre-pressure of 1 kN was exerted at a loading rate of 0.1 kN/s to make the press in tight contact with the rock piece, and then the rock piece was subjected to loading at a loading rate of 0.5 kN/s until it was demolished. AE and IR data were collected simultaneously within the loading procedure of the rock piece.

Results

Analysis of Uniaxial Compression Characteristics

Due to the difference of the piece itself, the data with large discreteness are eliminated, and the experiment data of G-D-2 and B-D-1 are selected. The stress-strain graphs and breakdown patterns of arid and water-soaked rock pieces are drawn as shown in Table 2 and Figure 4.

Table 2 Mechanical properties of uniaxial compression test.

Rock Piece	Peak Stress(MPa)	Peak Strain($\times 10^{-3}$)	Elasticity Modulus (GPa)
G-D-2	111.29	3.97	30.25
B-D-1	105.75	4.14	25.26
Relative Change	-4.98%	4.3%	-16.5%

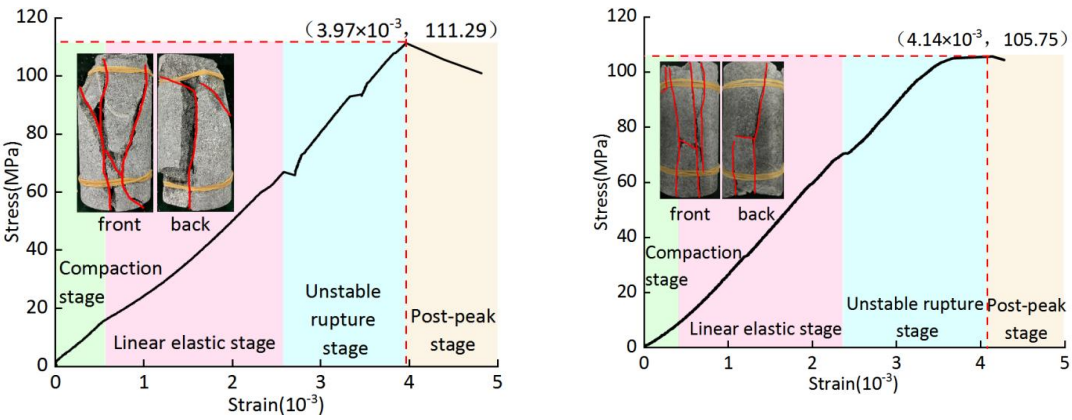

(a) arid rock pieces (b) water-soaked rock pieces

Figure 4 Stress-strain curve of arid and water-soaked rock.

The deformation and failure of rock pieces can be classified into the compaction stage, linear elastic stage, unstable rupture stage, and post-peak stage. As can be seen from Figure 4 (a) that the peak strength of arid rock pieces is 111.29 MPa, the peak strain is 0.003 97, and the elastic modulus is 30.25 GPa. At the beginning phase of loading, the stress-strain curve is basically linear, indicating that the arid rock piece is extremely dense, and hardly any natural micro-cracks can be found in the rock piece, and there is no obvious compaction phase. As the load increases further, the inner cracks in the rock start to extend and spread, after the stress exceeds the peak strength, the rock piece is instantaneously ruined and there is a loss of its bearing capacity. When the arid rock piece is destroyed, there is a penetrating tensile splitting crack on the front side, accompanied by local shear cracks, and a penetrating tensile crack on the back side. The whole rock piece is tensile splitting failure.

We can observe from Figure 4 (b) that the water-soaked rock piece has a peak strength of 105.75 MPa, the peak strain is 0.004 14, and the elastic modulus is 25.26 GPa. Compared with the arid rock piece, At the start, the stress-strain curve of the water-soaked rock piece exhibits a concave form, and the micro-cracks of the rock piece are gradually closed, and

an evident compaction phase exists. Within the linear elastic phase, the stress-strain curve appears to be nearly linear. When the stress keeps on rising, the yield strength of the rock piece is reached, and the unstable development phase is entered. The minute cracks within the rock piece grow rapidly and penetrate. After the stress exceeds the peak strength, the rock piece is instantaneously demolished and loses its carrying capacity. There are two penetrating tensile splitting cracks on the front of the water-soaked rock piece, one penetrating transverse shear crack between the two tensile cracks in the middle of the rock piece, and also on the backside surface of the rock piece lies one tensile crack that has penetrated. The fracture mode of the rock piece is tensile-shear failure.

Compared with arid rock pieces, the peak strength of water-soaked rock pieces decreased by 4.98%, the peak strain increased by 4.3%, and the elastic modulus decreased by 16.5%, indicating a significant reduction in rock stiffness, which may affect the deformation coordination and long-term stability of surrounding rock. Meanwhile, the failure mode showed more obvious shear failure characteristics, with significant increases in both main and secondary cracks, and more severe surface erosion. This phenomenon is due to water-induced damage to the rock. The rock pieces used in the test contain about 30% clay minerals. Under vacuum water-soaked conditions, some water molecules preferentially intrude into the clay mineral interlayers and particle interfaces, forming bound water films, which significantly reduce the cohesion and friction coefficient between particles, leading to easier shear slip of the rock under load. Macroscopically, this manifests as reduced peak strength and elastic modulus, and more obvious shear failure characteristics(Jia et al., 2018) .

Analysis of Infrared Radiation Characteristics

Average Infrared Radiation Temperature (AIR*T*)

During the course of uniaxial compression of rock, with the accumulation and dissipation of energy, the IR temperature field will change significantly. The infrared thermal imager is capable of gathering the IR temperature of the rock instantaneously and store it in the form of thermal image and temperature matrix. The series diagram of infrared thermal imagery is displayed by the special software Research IR.In order to better study the trend of thermal image and infrared temperature, the thermal image sequence diagram is derived into a computable temperature data matrix. The temperature matrix is processed by Matlab software, and the AIR*T* is selected to explore the precursor of rock fracture.

Under the circumstance of uniaxial compression loading, stress control is adopted. After loading, the acoustic-thermal signal acquisition system is turned on synchronously. Once the rock piece fails to sustain its load - bearing capacity, the loading and data acquisition are stopped. The AIR*T* is selected to depict the alteration of the surface temperature field throughout the fracture progress, and the AIR*T*-stress-time curves of arid and water-soaked rock pieces are plotted as illustrated in Figure 5.

As shown in Figure 5, the abrupt increase in AIR*T* upon loading (0.4 ℃ for arid rock pieces and 0.7 ℃ for water-soaked rock pieces) is primarily attributed to the thermoelastic effect. At the instant when axial load is abruptly applied, the rock undergoes instantaneous elastic deformation, and its internal lattice is compressed, leading to a reduction in entropy. This converts part of the mechanical energy into thermal energy, causing a transient temperature rise on the pieces surface (AIR*T* surge). Due to heat exchange (thermal convection and radiation) between the testing machine loading system and the rock pieces, as well as between the rock surface and the surrounding environment, the initially generated heat rapidly dissipates. Meanwhile, as the rock enters a sustained deformation phase, energy begins to be increasingly consumed by irreversible processes (crack compaction and closure, friction), causing the temperature rise effect due to purely elastic deformation to diminish, hence the observed sharp temperature drop. Assuming the thermoelastic effect generates the same amount of heat, the water-soaked rock pieces, due to the presence of water, have a greater overall thermal inertia and should exhibit a smaller temperature increase. However, the observed temperature rise is actually greater than that of arid rock pieces(0.7 ℃ vs. 0.4 ℃). This precisely demonstrates that the water-soaked rock pieces undergo more significant irreversible plastic deformation or crack closure during the initial loading stage. The heat generated by this portion of irreversible work superimposes on the thermoelastic effect, resulting in a higher initial temperature rise. Subsequently, the overall variation trend shows a decline-steep rise pattern, with a "*V*"-shaped inflection point occurring before rock failure. As shown in Figure 5 (a), the AIR*T* of arid rock pieces increases by 0.7 ℃ at the moment of rupture, which can serve as a precursor to instability failure of arid rock pieces. At the moment of rupture, the temperature of water-soaked rock pieces rises by 0.2 ℃. As shown in Figure 5 (b), when loaded to approximately 260 seconds, the AIR*T* of water-soaked rock pieces decreases from 24.2 ℃ to 23.7 ℃ indicating the occurrence of tensile micro-fractures in the water-soaked rock pieces at that time. In contrast, the arid

DOI: 10.5614/j.eng.technol.sci.2026.58.4.2

rock pieces exhibit only a minor fluctuation of 0.2 ℃ during this stage, indicating very limited crack propagation in the arid rock pieces.

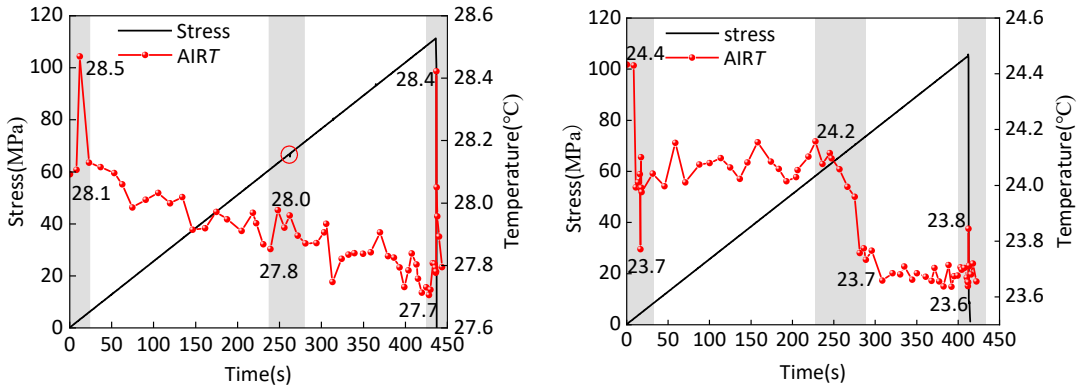

(a) arid rock pieces (b) water-soaked rock pieces

Figure 5 Temperature change curve under uniaxial compression.

Thermal Field Migration Distribution Map

Taking the first frame as the basic frame, the temperature difference is calculated by subtracting the temperature of the first frame from the temperature value of each frame of thermal imaging screen after loading with Matlab software, and output in the form of image. The thermal image transfer comparison is carried out at five moments of 0.5 σ_c, 0.7 σ_c, 0.9 σ_c, 0.98 σ_c and σ_c. Among them, σ_c is uniaxial compressive strength, and the distribution map of thermal field migration of arid and water-soaked rock pieces is drawn as presented in Figure 6.

As shown in Figure 6, during uniaxial compression, the evolution of infrared radiation temperature fields in arid and water-soaked gabbro exhibits distinct differences, visually revealing their different mechanisms of internal damage accumulation and energy transformation. In the figure, the horizontal axis represents the time change and the corresponding stress stage, and the color band of the vertical axis represents the temperature change (ΔT / °C) relative to the initial frame. Red indicates the temperature rise, and blue indicates the temperature drop.

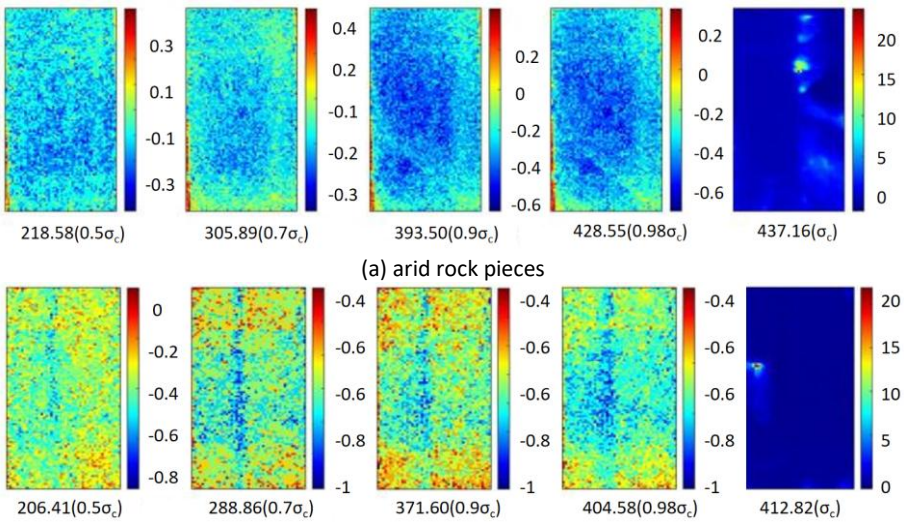

Figure 6 Thermal field migration distribution under uniaxial compression.

As shown in Figure 6 (a), for the arid rock pieces, during initial loading, a red high-temperature zone (ΔT > 0) appears in the lower left corner of the pieces, caused by localized friction or plastic deformation heating due to stress concentration. Most other areas display blue low-temperature zones (ΔT < 0), dominated by the thermoelastic cooling effect induced by tensile micro-fracture initiation within the rock. As stress increases, the low-temperature area continues expanding, reaching a maximum temperature drop of 0.7 °C at 0.98 σ_c . Immediately before failure, energy

releases rapidly as frictional heat, causing localized temperature spikes (up to 23.02 °C). Therefore, the precursor to failure in arid rock pieces mainly manifests as gradual expansion of low-temperature zones, reflecting damage accumulation primarily through tensile fracture.

As shown in Figure 6 (b), the thermal evolution characteristics of water-soaked rock pieces differ significantly. From initial loading, the pieces surface exhibits extensive blue low-temperature zones, with the maximum temperature drop area showing a distinct vertical band distribution. This phenomenon results from the combined effects of thermoelastic cooling and water evaporation heat absorption. As loading increases, this vertical low-temperature band not only expands in area but also shows continuously increasing absolute temperature drop values (reaching a maximum of 1.2°C at 0.98 σ_c). This vertical banded low-temperature zone indicates the formation of an interconnected tensile fracture zone within the water-soaked rock pieces. Consequently, the expansion of the low-temperature band and intensifying temperature drop can serve as more prominent instability precursors for water-soaked rock pieces.

In summary, the spatiotemporal evolution of infrared thermal imagery not only visualizes the rock damage process but also, through temperature signal differences (red temperature rise vs. blue temperature drop) and their spatial distribution patterns, profoundly reveals fundamental differences in energy absorption (dominated by tensile fracture and cooling) and energy release (dominated by frictional heating) mechanisms between arid and water-soaked rock pieces.

Analysis of AE Characteristics

Straightforwardly mirroring the interior impairment of the rock along with the developmental process of micro-crack origination and spread is what the AE activity is proficient at. Based on the AE parameters collected by arid and water-soaked rock pieces, the analysis data of AE amplitude ringing count and cumulative energy and time are obtained.

Figure 7 and Figure 8 are the AE parameter-stress-time curves of arid and water-soaked rock pieces. The AE amplitude density and AE ringing count of arid and rock pieces at the incipient phase of loading are small, indicating that micro-fractures occur less. This is because the arid gabbro itself is dense and there are few inner micro-cracks. As shown in Figure 7 (a) and Figure 8 (a), when the loading time is about 250 s, the AE amplitude density and AE ring count density increase sharply for the first time, and the amplitude is between 40 dB and 90 dB. The cumulative AE energy has the first transition, and the energy increment reaches 2×10^5 mv · μs, indicating that there is a slip adjustment of micro-cracks inside the rock at this phase, resulting in the first batch of cracks. At about 350 s, the AE amplitude density and AE ringing count increased significantly for the second time, and the amplitude and density decreased compared with the first increase, which was between 40 and 80 dB. The cumulative AE energy had a second transition, and the energy increment reached 0.5×10^5 mv · μs. After that, the AE amplitude stabilized at 40-65 dB until the third sudden increase of AE amplitude density and AE ringing count near the fracture phase. The cumulative AE energy had a third transition, and the energy increment was as high as 6×10^5 mv · μs. The cracks expanded rapidly and brittle failure occurred in arid rock pieces.

As shown in Figure 7(b) and Figure 8(b), at the beginning phase of loading, the AE amplitude density and AE ringing count of water-soaked rock pieces are small. After loading to 260 s, the AE amplitude density and AE ringing count increase significantly. The cumulative AE energy shows the first transition, and the energy increment reaches 5×10^5 mv · μs, and then the AE amplitude is stable at 40-70 dB. Before the rupture, the AE gets into the active period, the AE amplitude and density increase, and the cumulative AE energy keeps on grow. At the time when the peak strength is attained, the AE amplitude density and AE ringing count suddenly increase again, and the cumulative AE energy undergoes a second transition. The energy increment is as high as 12×10^5 mv · μs, and the rock piece failure exhibits plastic failure characteristics.

The cumulative AE energy of the arid and the water-soaked rock piece has undergone three and two transitions, respectively, of which the last transition is the most significant, and the cumulative AE energy increment of the water-soaked rock piece is twice that of the arid one, indicating that the water-soaked rock piece releases more energy than the arid one in the final failure phase, and the damage is more serious. In contrast to arid rock pieces, the cumulative AE energy curve of water-soaked rock pieces continues to grow after reaching a certain stress, and there is no obvious step-like feature. Rock pieces' failure mode shifts from brittle to plastic failure. The AE ringing count of arid and water-soaked rock pieces is foreshock-mainshock type.

When combined with the features of IR temperature, it is found that the features of AE are in line with the variation features of AIR*T* The stress-strain curve of arid rock pieces fluctuates around 250 s, and the cumulative AE energy transitions, as shown in Figure 8 (a). Due to the local heat release caused by micro-crack propagation, the AIR*T*

DOI: 10.5614/j.eng.technol.sci.2026.58.4.2

temperature changes by 0.2 °C. At about 360 s, the cumulative AE energy has a second small transition, and AIR*T* has a slight temperature rise. At the moment of destruction, AIR*T* and cumulative AE energy have a sudden increase at the same time, as shown in Figure 5 (a). The AIR*T* sudden drop and cumulative AE energy transition of the water-soaked rock piece near 260 s are largely because of the alteration of the interior framework of the rock caused by the migration of water molecules and the change of pore pressure, as shown in Figure 8 (b). At the moment of rupture, the AIR*T* and cumulative AE energy have increased suddenly, indicating that the micro-cracks in the near-ruptured rock piece extend and infiltrate, dislocation and friction occur, and the IR temperature increases, as shown in Figure 5 (b). The above phenomena indicate that the period of high AE activity exhibits strong synchronization with the inflection points in thermal response, which can serve as a precursor indicator for failure.

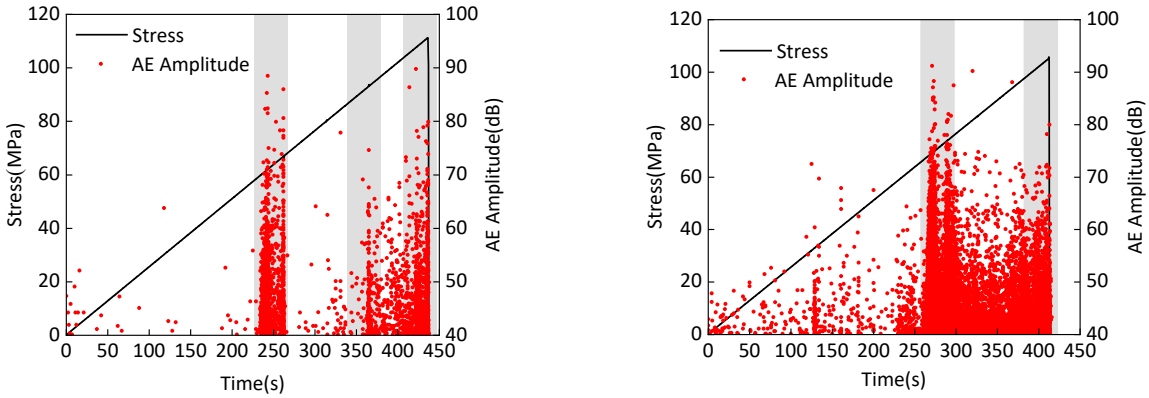

(a) arid rock pieces (b) water-soaked rock pieces

Figure 7 AE amplitude-stress-time-curve.

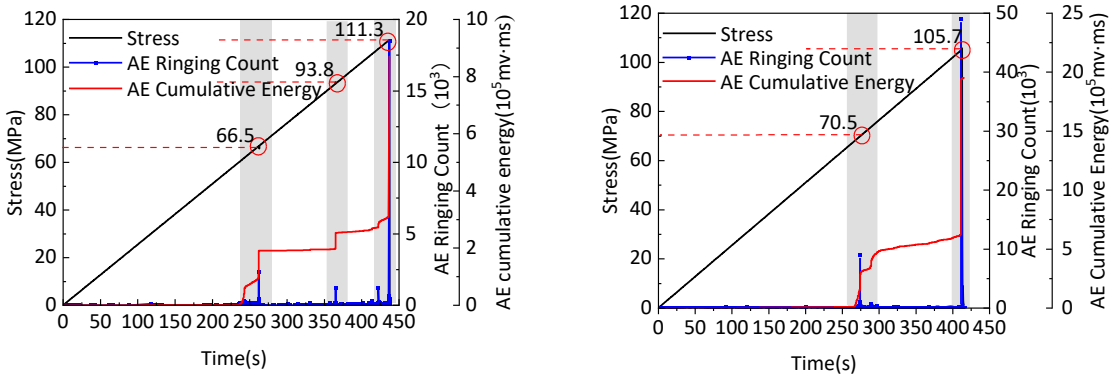

(a) arid rock pieces (b) water-soaked rock pieces

Figure 8 Ringing count-cumulative energy-stress-time curve.

Damage Evolution Law

Rock damage refers to the deterioration process of materials or structures caused by meso-structural defects, that is, the continuous generation and development of inner cracks and cracks under external loads, causing the worsening of mechanical properties. The interior framework of rock in nature is complex, so the damage theory is employed to investigate the evolutionary rule of rock damage. The selection of damage variables should be easy to measure and establish a relationship with macroscopic mechanical properties.

The aggregation of damage in rock micro - elements gives rise to the worsening of mechanical properties of rock pieces. The response of AE parameters is associated with the inner flaws of rock, which is an accompanying phenomenon of material damage.The damage variable that is founded on the cumulative AE ringing count is expressed as in Eq. (1) :

$$D = \frac{C_d}{C_0} \tag{1}$$

During the experiment, because the rock piece stops loading after losing the bearing capacity, The rock piece is usually not fully damaged, often failing to reach 100% damage.. Therefore, the damage variable of Eq.(1) is modified as in Eq. (2):

$$D_{AE} = D_U D = \left(1 - \frac{\sigma_c}{\sigma_p}\right)\frac{C_d}{C_0} \tag{2}$$

Under uniaxial compression, rock damage evolution has roughly three phases, as shown in Figure 9. Firstly, initial damage phase : the D_{AE} is almost 0 and the slope of the curve is 0. Due to the fact that the rock piece is in the compaction phase or linear elastic phase, hardly any micro-cracks form, and the inner damage does not develop.Secondly, damage stable development phase: the damage of rock piece rises gradually, but the value of damage variable D_{AE} is still very small, signifying that the micro-cracks in the rock piece are tightly compressed and sealed at this phase, and merely a bit of damage is generated. Finally, damage acceleration phase: D_{AE} shoots up to the crucial value, the micro-cracks inside the rock piece expand quickly, penetrate and form macroscopic cracks, and the bearing capacity quickly drops.

From Figure 9, the change processes of arid and water-soaked rock pieces are alike in the initial and accelerated damage phases. The damage in the initial damage phase is almost 0, the inner damage of the rock piece does not develop, and the damage in the hastened damage development phase rapidly increases to the crucial value, and the bearing capacity of the rock piece vanishes. However, there is a slight difference in the phase of damage's stable growth. The damage of arid rock pieces increases rapidly in the phase of stable development of damage, and then develops steadily, while the D_{AE} curve of water-soaked rock pieces rises steadily at this phase. This results from the random pores distribution in arid rock pieces. At this phase, rock particles generate dislocations or micro-crack propagation to release strain energy, resulting in a sudden increase in damage. After water-soaked rock pieces are infiltrated by ionic water, the inner particles are connected by bound water, and no dislocation motion occurs, so the damage develops steadily.

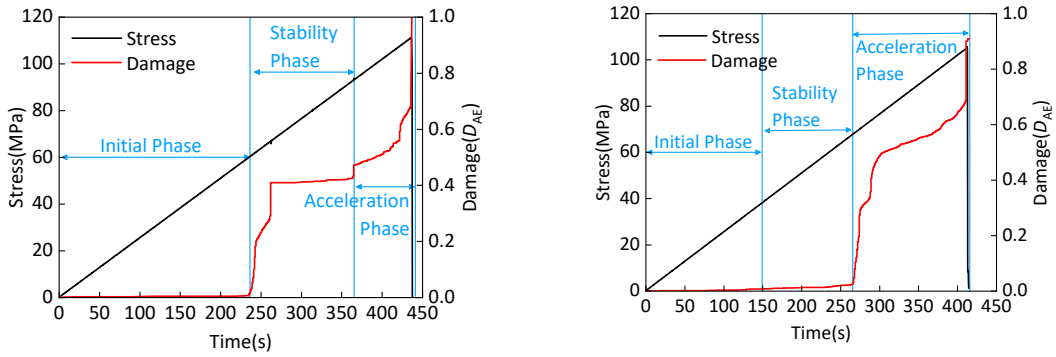

(a) arid rock pieces (b) water-soaked rock pieces

Figure 9 Damage-stress-time curve of rock piece.

Eq.(3) shows the association between the damage variable and the micro-element damage probability density.

$$\frac{dD}{d\varepsilon} = \varphi(\varepsilon) \tag{3}$$

Rock is a special geological material, which has numerous pores, fissures and joints. Its physical and mechanical properties are usually anisotropic and nonlinear. Random defects exist in rock materials, so rock damage can be described by statistical distribution law. It is assumed that rock strength obeys Weibull distribution (Wu & Zhang, 1996) , and its probability density function as:

$$\varphi(\varepsilon) = \frac{m}{F}\left(\frac{\varepsilon}{F}\right)^{m-1} exp\left[-\left(\frac{\varepsilon}{F}\right)^{m}\right] \tag{4}$$

From Eq.(3) and Eq.(4) :

$$D = \int_0^{\varepsilon} \varphi(x)\, dx = \frac{m}{F}\int_0^{\varepsilon}\left(\frac{x}{F}\right)^{m-1} exp\left[-\left(\frac{x}{F}\right)^{m}\right] dx = 1 - exp\left(-\left(\frac{\varepsilon}{F}\right)^{m}\right) \tag{5}$$

Drawing on Lemaitre's strain equivalence principle, the constitutive relation can be defined as:

$$\sigma = E_0\varepsilon(1 - D) \tag{6}$$

The constitutive relation of rock damage in Eq. (7) is obtained from Eq.(5) and Eq.(6):

$$\sigma = E_0\varepsilon\, exp(-(\frac{\varepsilon}{F})^{m}) \tag{7}$$

DOI: 10.5614/j.eng.technol.sci.2026.58.4.2

The parameters *m* and *F* can be decided by the peak strength point (ε_c, σ_c) on the stress-strain curve. The slope of the uniaxial compression curve at the peak strength point is 0, so in Eq. (8) :

$$\frac{d\sigma}{d\varepsilon}|_{\varepsilon=\varepsilon_c} = E_0\, exp\left[-(\frac{\varepsilon}{F})^m\right]\left[1-\frac{m}{F}\varepsilon(\frac{\varepsilon}{F})^{m-1}\right] = 0 \tag{8}$$

At the same time, the relationship is satisfied at the peak point (ε_c, σ_c) in Eq. (9):

$$\sigma_c = E_0\varepsilon_c\, exp\left[-\left(\frac{\varepsilon_c}{F}\right)^m\right] \tag{9}$$

The *m* and *F* can be acquired through combining Eqs.(8) and (9). The obtained damage statistical parameters are substituted into the formula to obtain the statistical damage formula of rock pieces. The comparative analysis of the theoretical model and the experimental findings is displayed in Figure 10. The damage constitutive theoretical curve is found to be in line with the experimental curve, showing the process of micro-crack generation, development and failure in rock. Future research could incorporate dynamic damage models that account for microcrack interactions and the evolution of damage thresholds, or combine plastic theories that better describe post-peak behavior, to further enhance the predictive accuracy of constitutive relations during both the peak and post-peak stages.

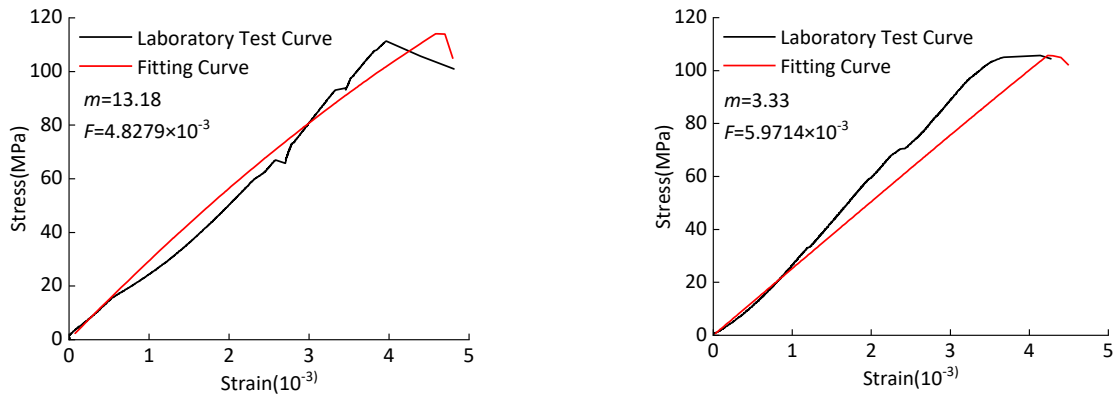

(a) arid rock pieces (b) water-soaked rock pieces

Figure 10 Comparison between theoretical and experimental curves of damage constitutive curves.

Discrete Element Simulation

Establishment of Particle Flow Model

The indoor experiment can only observe the macroscopic fracture of the rock, and it is impossible to expose the extension and penetration of the micro-cracks in the inner structure of the rock from the microscopic perspective. Based on the particle flow theory, it is assumed that the rock is composed of rigid spheres, and its movement process conforms to Newton 's law of motion. By adjusting the microscopic parameters, the failure mode and peak strength of the numerical rock piece are similar to the macroscopic mechanical characteristics of the indoor experiment rock piece for revealing the start and spread process of the inner micro-cracks during rock failure. This model between particles selected in this paper is a parallel bond model, and the softening of rock pieces by water is simulated by changing the parallel bond multiplier λ.

A 50-mm-diameter, 100-mm-high cylindrical piece was made. A total of 16832 particles were generated. The lowest limit of the radius of the generated particles was 1 mm, and the particle size ratio was 1.66. A total of 45922 bonds were generated when the numerical model reached equilibrium. The particle flow modeling process is shown in Figure 11. Combined with the stress-strain curve, macroscopic mechanical parameters and failure mode obtained by indoor uniaxial experiment, the relevant parameters are adjusted repeatedly by trial and error method, and the specific mesoscopic parameters of rock pieces are finally obtained as shown in Table 3. Table 3 shows the comparison of stress - strain curves from indoor experiments and numerical simulations of arid and water-soaked rock pieces. Taking the stress drop to 70 % of the peak stress as the stopping condition of numerical simulation, for arid rock piece, the parallel bond radius multiplier is 1.0; The parallel bond radius multiplier for the water-soaked rock pieces was calibrated through a trial-and-error approach based on the parameters of the dry model. Starting from an initial λ value of 0.99, it was progressively reduced to 0.95 while conducting uniaxial compression simulations. The resulting peak strength and elastic modulus were compared with experimental data from water-soaked pieces. The optimal λ value was ultimately determined to be 0.97, while all other mesoscopic parameters remained unchanged.

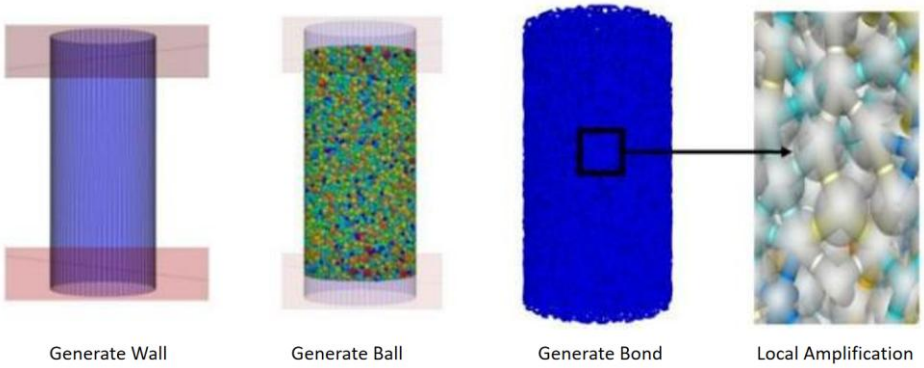

Figure 11 PFC3D numerical model establishment process.

Table 3 Mesoscopic parameters of PFC3D numerical model.

Mesoscopic Parameters	Numerical Value	Mesoscopic Parameters	Numerical Value
Particle Density(kg·m^{-3})	2900.0	Parallel Bond Stiffness Ratio	1.5
Minimum Particle Size(mm)	1.0	Solid Friction Factor	0.5
Particle Size Ratio	1.66	Parallel Bond Tensile Strength(MPa)	93.15
Effective Modulus(GPa)	29.3	Parallel Bond Micro Cohesion(MPa)	81.0
Parallel Bond Modulus(GPa)	29.3	Parallel Bond inner Friction Angle(°)	30.0
Stiffness Ratio	1.5	Normal Stress Update Mode	1.0

As shown in Figure 12, the errors of uniaxial compressive peak strength under arid and water-soaked conditions are 1.26 % and 2.79 %, respectively, and the errors of elastic modulus are 0.58 % and 3.59 %, respectively. The macroscopic parameters of rock acquired through numerical simulation are extremely near those of laboratory experiments. As shown in Figure 13, comparative analysis demonstrates that the numerical simulation not only reproduces the predominantly tensile crack (green) failure pattern observed in arid rock pieces, but also successfully captures the extensively developed shear cracks (red) and the resulting composite failure mode formed in conjunction with tensile cracks in water-soaked rock pieces. This provides further mesoscopic evidence that water-induced softening promotes the transition of failure mode toward shear dominance.

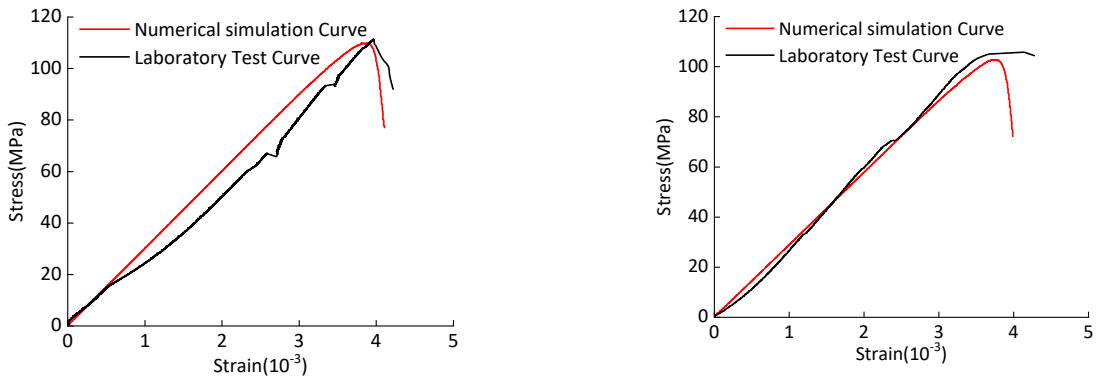

(a) arid rock pieces (b) water-soaked rock pieces

Figure 12 Comparison of stress-strain curves of rock pieces.

(a) arid rock pieces (b) water-soaked rock pieces

Figure 13 Comparison between experemintal and simulated failute patterns of rock pieces.

DOI: 10.5614/j.eng.technol.sci.2026.58.4.2

Numerical Simulation Results Analysis

By analyzing the progression of micro - cracks in arid and water-soaked states, the origination and progression of tensile and shear cracks under arid and water-soaked conditions are investigated individually, and the effect of groundwater concerning the failure pattern of gabbro is discussed.

Figure 14 is the growth illustration of the count of cracks in arid and water-soaked rock pieces during loading. Tensile and shear micro-cracks occur simultaneously in arid and water-soaked rock pieces. At the beginning of loading, the count of cracks is rather scarce. As the stress rises, the rock piece enters the phase of unstable fracture, and the amount of shear cracks is more than that of tensile cracks. When the rock piece is finally destroyed, the amount of tensile cracks is more than that of shear cracks. The amount of shear cracks is 3684 when the arid rock piece is eventually ruined, and the amount off shear cracks is 3755 when the water-soaked rock piece is finally destroyed. The proportion of the amount of shear cracks in the water-soaked rock piece to the total amount off cracks surpasses that of the arid rock piece. Therefore, the failure pattern of the rock piece progressively transforms from the tensile splitting failure in the arid state to the tensile-shear failure.

As shown in Figure 14, for the arid rock pieces (Fig. 14a), the stress-strain curve exhibits a steep post-peak brittle drop characteristic. Correspondingly, the total crack curve shows a sharp increase near the peak point, with tensile cracks consistently significantly outnumbering shear cracks. This indicates that the failure is dominated by the rapid propagation and coalescence of tensile cracks, ultimately forming macroscopic tensile splitting surfaces. For the water-soaked rock pieces (Fig. 14b), the proportion of shear cracks throughout the loading process is higher than that in the arid rock pieces. This demonstrates that the presence of water preferentially weakens the bonding strength between rock particles, significantly reducing the shear resistance of the pieces. Consequently, under load, the water-soaked rock pieces are more prone to shear slip, with microcrack evolution manifesting as a continuous, stable growth of shear cracks. After peak stress, these shear cracks coalesce with tensile cracks to form interconnected shear fracture zones, ultimately leading to macroscopic tensile-shear composite failure.

The softening effect of water not only reduces the macroscopic mechanical response of the gabbro but also, by altering the evolution path and type distribution of mesoscopic cracks, promotes a transition in failure mode from brittle tensile splitting in the arid state to tensile-shear composite failure in the water-soaked state.

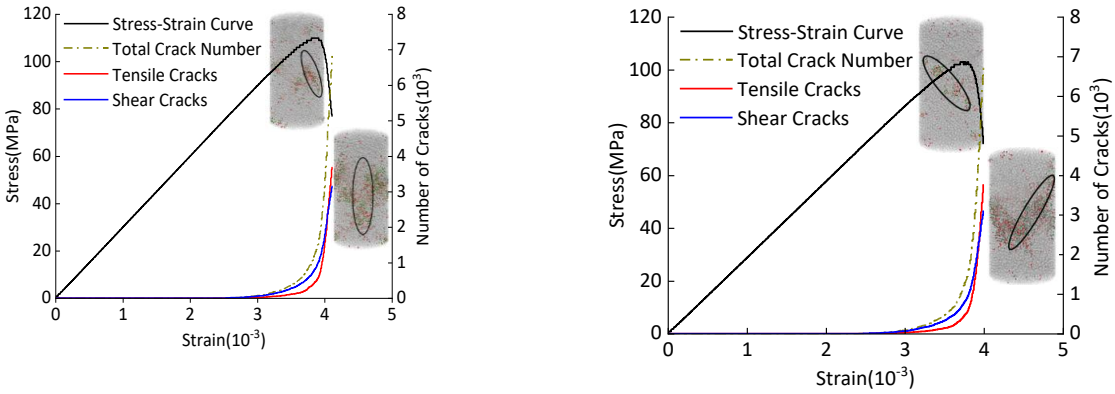

(a) arid rock pieces (b) water-soaked rock pieces

Figure 14 Relationship curve of crack quantity and strain of rock piece under uniaxial compression.

Discussion

The results indicate that water soaking leads to a 4.98% reduction in the peak strength of gabbro and a significant 16.5% decrease in the elastic modulus. This phenomenon is closely related to the mineral composition of gabbro, which contains 31.8% clay minerals. Clay minerals have strong hydrophilicity; when water molecules infiltrate the rock interior, they form bound water films on the surfaces of mineral particles and between layers, reducing the cohesion and friction coefficient between particles (Jia et al., 2018). Compared with existing studies on sandstone and limestone (Cheng et al., 2022; Fan et al., 2022), the peak strength reduction of gabbro due to water soaking is relatively mild, which may be attributed to its high content of non-clay minerals (68.2%), forming a stable load-bearing framework that mitigates the weakening effect of water to a certain extent. However, the significant decrease in elastic modulus suggests that water has a more pronounced impact on the stiffness of gabbro, which may lead to increased deformation of surrounding

rock in engineering projects and affect long-term stability. Therefore, in railway tunnel construction and other projects involving gabbro formations, special attention should be paid to the influence of groundwater on rock stiffness, and corresponding reinforcement measures should be taken to ensure structural safety.

The synchronous monitoring of acoustic emission (AE) and infrared radiation (IR) reveals the damage evolution process of gabbro. Both arid and water-soaked gabbro exhibit a foreshock-mainshock pattern in AE parameters, which is consistent with the crack initiation, propagation, and coalescence process. The cumulative AE energy of water-soaked gabbro during final failure is twice that of arid gabbro, indicating more severe energy release and damage. This is because water weakens the interparticle bonds, making microcracks easier to propagate and coalesce, resulting in more intense energy release during failure. In terms of IR response, the average infrared radiation temperature (AIRT) curve of gabbro during loading shows a "V"-shaped trend, which is a common precursor to rock failure. For water-soaked gabbro, the initial temperature rise due to the thermoelastic effect is higher than that of arid gabbro, which is caused by more significant irreversible deformation (such as crack compaction and closure) during the initial loading stage. The thermal field migration distribution map further shows that water-soaked gabbro forms vertical banded low-temperature zones during loading, which is the result of the combined effects of thermoelastic cooling and water evaporation heat absorption, and can be used as a prominent precursor for instability. This is consistent with the findings of Cao et al. (2022) that water soaking enhances rock infrared emission, but the unique vertical low-temperature band distribution of gabbro provides new insights for the identification of failure precursors in water-soaked hard rocks.

The strong synchronization between AE active periods and IR temperature inflection points confirms the complementary advantages of acoustic-thermal cooperative monitoring. AE can accurately capture the initiation and energy release of internal microcracks, while IR can visually reflect the surface thermal field evolution caused by energy dissipation. This cooperative monitoring method is superior to single monitoring techniques and provides a reliable technical means for real-time safety monitoring and disaster early warning in geotechnical engineering. The PFC particle flow simulation reveals the mesoscopic mechanism of water-induced failure mode transition in gabbro. The simulation results show that the number and proportion of shear cracks in water-soaked gabbro are significantly higher than those in arid gabbro, leading to the failure mode shifting from tensile splitting to tensile-shear composite failure. This is because water weakens the parallel bond strength between particles (simulated by the parallel bond multiplier λ=0.97), making the rock more prone to shear slip under load. Compared with the numerical simulation results of red sandstone by Zhao et al. (2021), the failure mode transition of gabbro due to water soaking is more obvious, which may be related to the differences in mineral composition and microstructure between rocks. The consistency between the simulation results and indoor experiment data (with peak strength and elastic modulus errors within 3%) verifies the reliability of the numerical model, providing an effective method for studying the mesoscopic damage mechanism of rocks that is difficult to observe in indoor experiments.

Conclusion

This study investigates the mechanical properties, acoustic-thermal response, and failure mechanisms of gabbro under arid and water-soaked conditions using uniaxial compression tests, acoustic emission-infrared radiation (AE-IR) monitoring, and Particle Flow Code (PFC) simulations. Key conclusions are as follows: Water significantly degrades the mechanical performance of gabbro: its peak strength decreases by 4.98% and elastic modulus by 16.5%. Moreover, the failure mode transitions from tensile splitting (in the arid state) to tensile-shear failure (in the water-soaked state). This degradation is driven by water weakening the bonds between particles, which increases the number of shear cracks and alters the failure path. Cooperative AE-IR monitoring enables reliable early warning of gabbro failure: AE effectively captures the initiation of internal microcracks and the release of associated energy, while IR reflects the evolution of the surface thermal field during loading. The temporal consistency between AE activity and IR temperature inflections provides robust support for safety monitoring in geotechnical engineering. PFC simulations accurately replicate the macroscopic mechanical behavior and failure mode of gabbro. They further reveal the mesoscopic mechanism underlying water-induced failure and compensate for the limitation of laboratory experiments in observing microcrack evolution. Future research will focus on the effects of varying moisture contents and complex stress paths, optimize damage constitutive models, and advance the application of these findings in practical geotechnical engineering projects.

Nomenclature

C_0	The cumulative AE ringing count of rock at the final failure
C_d	The cumulative AE ringing count of rock at a certain moment in the loading process
D_U	Critical damage

DOI: 10.5614/j.eng.technol.sci.2026.58.4.2

E_0	Elastic modulus
F	Parameters associated with the form, size and inner flaw distribution of rock pieces
m	Parameters associated with the form, size and inner flaw distribution of rock pieces
σ	Stress
σ_c	Residual strength
σ_p	Peak strength
ε	Strain

Acknowledgements

This research was funded by Shaanxi Provincial Innovation Capability Support Program Project (2020TD-005) and 2023 CRBC Science and Technology Research Projects (2023-zlkj-03).

Compliance with ethics guidelines

The authors declare they have no conflict of interest or financial conflicts to disclose.

This article contains no studies with human or animal subjects performed by the authors.

References

Cao, K., Ma, L., Wu, Y., Spearing, A. J. S. (Sam), Khan, Naseer. M., Hussain, S., & Ur Rehman, F. (2022). Statistical damage model for dry and saturated rock under uniaxial loading based on infrared radiation for possible stress prediction. *Engineering Fracture Mechanics, 260*, 108134. https://doi.org/10.1016/j.engfracmech.2021.108134

Chen G, Li T, Wang W, Zhu Z., Chen Z., & Tong O. (2024). Weakening effects of the presence of water on the brittleness of hard sandstone. *Bulletin of Engineering Geology and the Environment, 78*(3), 1471-1483. https://doi.org/10.1007/s10064-017-1184-3

Cheng, Y., Song, Z., Liu, Z., Tian, X., Qian, W., Lu, X., & Yang, T. (2024). Micro-cracking morphology and dynamic fracturing mechanism of natural brittle sandstone containing layer structure under compression. *Construction and Building Materials, 425*, 136051. https://doi.org/10.1016/j.conbuildmat.2024.136051

Cheng, Y., Song, Z., Yang, T., Han, J., Wang, B., & Zhang, Z. (2022). Investigating the aging damage evolution characteristics of layered hard sandstone using digital image correlation. *Construction and Building Materials, 353*, 128838. https://doi.org/10.1016/j.conbuildmat.2022.128838

Fan, S., Song, Z., Xu, T., & Zhang, Y. (2022). Investigation of the microstructure damage and mechanical properties evolution of limestone subjected to high-pressure water. Construction and Building Materials, 316, 125871. https://doi.org/10.1016/j.conbuildmat.2021.125871

Ge, Z., & Sun, Q. (2021). Acoustic emission characteristics of gabbro after microwave heating. *International Journal of Rock Mechanics and Mining Sciences, 138*, 104616. https://doi.org/10.1016/j.ijrmms.2021.104616

Huang S, He Y, Liu X, & Xin Z. (2021). Experimental investigation of the influence of dry-wet, freeze-thaw and water immersion treatments on the mechanical strength of the clay-bearing green sandstone. International Journal of Rock Mechanics and Mining Sciences, 138: 104613. https://doi.org/10.1016/j.ijrmms.2021.104613

Huang S., Yu S. (2022). Effect of water saturation on the strength of sandstones: Experimental investigation and statistical analysis. *Bulletin of Engineering Geology and the Environment, 81*(8), 323. https://doi.org/10.1007/s10064-022-02822-9

Jia H, Wang T, Xiang W, Tan L, Shen Y, Yang G. (2018). Influence of water content on the physical and mechanical behaviour of argillaceous siltstone and some microscopic explanations. *Chinese Journal of Rock Mechanics and Engineering, 37*(7), 1618-1628. 10.13722/j.cnki.jrme.2017.1037

Li W, Cao J, Liu Z, Ma L., Li S., Liu Y., Yue L., & Wang J. (2025). Numerical Simulation of Water-Sand Flow Characteristics in Fractured and Porous Media Within Coal Mining Areas. *Mine Water and the Environment, 44*, 338-351. https://doi.org/10.1007/s10230-025-01047-y

Liu, X., Jia, H., Wang, C., Han, L., & Sun, Q. (2024). Dynamic behavior of fractured gabbro treated by high temperatures. Heliyon, 10(19), e38934. https://doi.org/10.1016/j.heliyon.2024.e38934

Liu, X., Liang, Z., Zhang, Y., Liang, P., & Tian, B. (2018). Experimental study on the monitoring of rockburst in tunnels under dry and saturated conditions using AE and infrared monitoring. *Tunnelling and Underground Space Technology, 82*, 517‑528. https://doi.org/10.1016/j.tust.2018.08.011

Ma, L., Muhammad Khan, N., Feroze, T., Sazid, M., Cao, K., Hussain, S., Gao, Q., Alarifi, S. S., & Wang, H. (2024). Prediction of rock loading phases using average IR temperature under shear and uniaxial loading. *Infrared Physics & Technology, 136*, 105084. https://doi.org/10.1016/j.infrared.2023.105084

Muhammad Khan, N., Ma, L., Feroze, T., Wang, D., Cao, K., Gao, Q., Wang, H., Hussain, S., Zhang, Z., & Alarifi, S. S. (2023). Investigating average IR temperature characteristics during shear and tensile cracks in sandstone under different water contents. I*nfrared Physics & Technology, 135,* 104968. https://doi.org/10.1016/j.infrared.2023.104968

Song, Z., Xu, X., Tian, X., Wang, T., Song, W., & Cheng, Y. (2024). Study on acoustic emission fracture response and constitutive model of layered sandstone. *Geomechanics and Engineering, 39*(2), 157‑170. https://doi.org/10.12989/gae.2024.39.2.173

Wu Z, Zhang C. (1996). Investigayion of Rock Damage Model and its Mechanical Behaviour. *Chinese Journal of Rock Mechanics and Engineering,* 1, 55-61.

Xiao, F., He, J., Liu, Z., Shen, Z., & Liu, G. (2019). Analysis on warning signs of damage of coal pieces with different water contents and relevant damage evolution based on AE and infrared characterization. *Infrared Physics & Technology, 97*, 287‑299. https://doi.org/10.1016/j.infrared.2019.01.007

Xu R., Hu Y., Yan Z., Zhao Y., & Li Z. (2024). Experimental investigation on the effect of water saturation on the failure mechanism and acoustic emission characteristics of sandstone. *International Journal of Geomechanics, 24*(6), 04024102. https://doi.org/10.1061/IJGNAI.GMENG-8526

Yu Y., Guo W., Liu J., Wu Z., & Xu D. (2025). Experimental-simulation analysis on mechanical degradation and energy evolution characteristics of sandstone under water-rock coupling effects. *Scientific Report, 15*(1), 18713. https://doi.org/10.1038/s41598-025-02557-z

Zhang, H., Lu, K., Zhang, W., Zhou, Y., Yang, G., Li, J., & Huang, C. (2023). A comprehensive study of damage characteristics and AE response mechanism of sandstone with different water contents. *Engineering Fracture Mechanics, 288*, 109392. https://doi.org/10.1016/j.engfracmech.2023.109392

Zhao K., Yang D., Zeng P., Huang Z., & Teng T. (2021). Effect of water content on the failure pattern and acoustic emission characteristics of red sandstone. *International Journal of Rock Mechanics and Mining Sciences, 142*, 104709. https://doi.org/10.1016/j.ijrmms.2021.104709

Zhou, S., Sun, Q., Zhang, H., Meng, H., Gao, Q., & Zhou, Y. (2023). Elemental dissolution characteristics of granite and gabbro under high-temperature water-rock interactions. *Science of The Total Environment, 897*, 165455. https://doi.org/10.1016/j.scitotenv.2023.165455

Zhu, J., Chen, X., Chen, J., Chen, H., & Pak, R. Y. S. (2024). Effect of cyclic loading level on mechanical response and microcracking behavior of soaked sandstones: Correlation with water weakening phenomenon. *Engineering Geology, 340*, 107667. https://doi.org/10.1016/j.enggeo.2024.107667

Manuscript Received: 24 July 2025
1st Manuscript Revision Received: 1 October 2025
2nd Manuscript Revision Received: 10 November 2025
Accepted Manuscript: 14 January 2026